OPEN ACCESS AEN NEA

The Clay Minerals Society Workshop Lectures Series, Vol. 21 (2016), Chapter 6, 65–77

MICROSCOPIC X-RAY IMAGING TECHNIQUES APPLIED TO MINERAL SYSTEMS AND CATALYST PARTICLES

J.F.W. Mosselmans[1,*], C.I. Pearce[2], W.R. Bower[3], R.A.D. Pattrick[3], S.W.T. Price[1], A.M. Beale[4,5], A.P. Sims[2], and L. Barrio[6]

[1]*Science Division, Diamond Light Source, Harwell Campus, Didcot, Oxon OX11 ODE, UK*
[2]*School of Chemistry and Dalton Nuclear Institute, University of Manchester, Manchester M13 9PL, UK*
[3]*School of Earth, Atmospheric and Environmental Sciences, University of Manchester, Manchester M13 9PL, UK*
[4]*UK Catalysis Hub, Research Complex at Harwell, Harwell Campus, Didcot OX11 0FA, UK*
[5]*Department of Chemistry, University College London, 20 Gordon Street, London WC1H 0AJ, UK*
[6]*Velocys Technologies Ltd., 115e Olympic Avenue, Milton Park, Abingdon OX14 4SA, UK*
[*]*e-mail: fred.mosselmans@diamond.ac.uk*

The development of complementary imaging techniques at beamline I18 at Diamond Light Source (Didcot, UK) to investigate the microstructure of inorganic materials is described. In particular, the use of X-ray micro-imaging techniques to understand the effect of alpha radiation on phyllosilicates, and the nature of individual catalytic particles are reported. Micro X-ray diffraction (μXRD) studies of the former materials have shown structural changes that will affect their adsorption properties, while the chemistry of the catalyst particles has been investigated using micro X-ray fluorescence, μXRD and μX-ray absorption near-edge structure mapping. The distribution of a Mo-promoted Pt nitrobenzene hydrogenation catalyst has shown that some of the Pt penetrated to the core of the particle and has the same chemistry as the bulk of the Pt located on the outside of the particle. The phase distribution in an as-prepared Re-Ti-promoted Co Fischer-Tropsch catalyst is reported.

1. Introduction

X-ray absorption spectroscopy (XAS) and X-ray diffraction (XRD) are known to give structural information on different length scales; XAS provides local electronic and structural information about a particular element in a sample, while XRD provides long-range order of the lattice planes in a crystalline material, providing information on crystal structure and probing both phase changes and structural damage. Hence, by combining the two techniques in association with X-ray fluorescence (XRF) chemical

© Copyright 2016, The Clay Minerals Society
DOI: 10.1346/CMS-WLS-21.6

mapping, a comprehensive characterization of a material is obtained. Furthermore, the use of a micro- or nano-beam enables heterogeneity to be examined at the scale of the beam size.

The advent of third-generation synchrotron sources with much lower emission characteristics has led to the application of synchrotron microfocus X-ray imaging techniques across the full range of science in the last two decades (*e.g.* Marcus, 2010). The use of these techniques in environmental science was reviewed by Lombi and Susini (2009) and by Fittschen and Falkenberg (2011). Use of these techniques in mineral studies is also widespread and includes work on Ni-bearing laterites (Roque-Rosell *et al.*, 2010) and the association of thallium with birnessite (Peacock and Moon, 2012).

Phyllosilicates are of critical importance to the international safety cases underpinning the construction of long-term geological disposal facilities (GDF) for highly radioactive wastes. These safety cases have to satisfy the appropriate regulators of the safety and security of all aspects in the development of a geological disposal facility before construction of the GDF can begin. This includes safety during construction, operation, and in the long term after the facility has been closed. Biotite is a ubiquitous component of the crystalline host rocks (granitic lithologies and gneiss) being considered for permanent geological isolation, and phyllosilicate structures are expected to retard radionuclide transport following eventual waste-canister failure, accumulating radiation damage in the process. Biotite mica is a trioctahedral phyllosilicate, characterized by repeated tetrahedral Si sheets surrounding metal-rich octahedral sheets; these TOT layers are bound together weakly by interlayer cations (typically K^+). Montmorillonite is a dioctahedral phyllosilicate with a similar layer structure to that of biotite but with a hydrated interlayer containing weakly bound cations, and a particle size of <2 μm. Montmorillonite is the main component of bentonite which will form the backfill surrounding high-level radioactive wastes in GDFs (Lee and Tank, 1985; Allard and Calas, 2009; Savage and Arthur, 2012).

In the field of heterogeneous catalysis, recent developments in diffraction-based X-ray imaging methods such as pencil beam and microfocus X-ray diffraction computed tomography (μXRD-CT) have been demonstrated to provide a deeper understanding of phase distribution of a catalyst over a support (*e.g.* Basile *et al.*, 2010; Bleuet *et al.*, 2008; Jacques *et al.*, 2011; Beale *et al.*, 2014). The XAS and/or XRF analysis provide detail on the chemical distribution and nature of the catalytic species (Ruiz-Martinez *et al.*, 2013).

On the microfocus spectroscopy I18 beamline at Diamond a range of synchrotron imaging techniques has been employed in recent years to study both mineralogical and catalytic systems. The advantages of third-generation synchrotron sources and the range of science which they enable have been highlighted recently with respect to the 'Diamond' facility (Materlik *et al.*, 2015). In particular, the use of fluorescence XANES mapping in combination with XRD mapping has been pioneered on the beamline (Brinza *et al.*, 2014). Here, details of recent experiments from I18 are reported including imaging investigations of the layer silicates biotite and montmorillonite (the latter being the main component of bentonite), after they had been subjected to

controlled doses of alpha-particle radiation and 3D imaging of catalyst particles including one previously reported study (Price *et al.*, 2015a).

2. Experimental

Beamline I18 at Diamond has a minimum spot size of ~2 μm and an energy range from 2 to 20.6 keV (Mosselmans *et al.*, 2009). Focusing is provided by a pair of mechanically bent Kirkpatrick-Baez mirrors by means of which the size of the beam can be tailored to sample requirements. Fluorescence X-rays were collected by a Vortex ME-4 Silicon Drift detector. Diffraction images were recorded using a Photonic Sciences Ltd. CMOS-based camera.

2.1. Phyllosilicates

Study of the effects of radiation damage on the properties of clay minerals (montmorillonite) and micas (biotite) is essential to determine their performance in a GDF and requires spatially resolved structural analysis (Bower *et al.*, 2016). Two phyllosilicate samples were prepared for α-radiation damage using the Dalton Cumbrian Facility (DCF) pelletron (Leay *et al.*, 2015): (1) a thin (<40 μm) sheet of biotite extracted from a large single crystal from Iveland, southern Norway (Rickwood, 1981); and (2) the montmorillonite SCa-3, obtained from the Source Clays Repository of The Clay Minerals Society, was pressed into a pellet (9 ton, 0.3 g, 13 mm) with a density of ~2 g cm^{-3} (representative of compacted bentonite), mounted on a glass slide over a hole, and thinned to ~100 μm. The pelletron's focused ion beam has a Gaussian profile in real space with respect to particle fluence. Thus, one sample accumulated a range of doses along the beam radius of 6.75 mm, permitting the analysis of relative changes in damage accumulation from a single sample. Along its length the samples were exposed to doses of 0 to 1×10^{16} 5 MeV $^4He^{2+}$ ions (Bower *et al.*, 2016).

After irradiation the sample was examined on beamline I18 using μXRD and μXANES. A 2 μm ×5 μm beam spot with a beam energy of 12 keV for the biotite and 6.7 eV for montmorillonite was used to collect XRD images every 30 μm in a track across the damaged zones. The XRD images were analysed in the program *DAWN* (Basham *et al.*, 2015). For μXANES, Fe K-edge XAS spectra were acquired along the same traverse as the μXRD data. All XAS data were analyzed in the Demeter Suite (Ravel and Newville, 2005).

2.2. Catalysts

Two different catalyst particles were studied. A Mo-promoted Pt carbon-based catalyst (Pt-Mo/C) (BASF SE) used in the selective hydrogenation of nitrobenzene and a 1% Re and 5% Ti promoted 10% Co oxide on silica (Velocys Technologies Ltd), which is used as a Fischer-Tropsch catalyst. The particle size for both catalysts varied between 80 and 200 μm. The imaging reported here was on the as-prepared catalyst in both

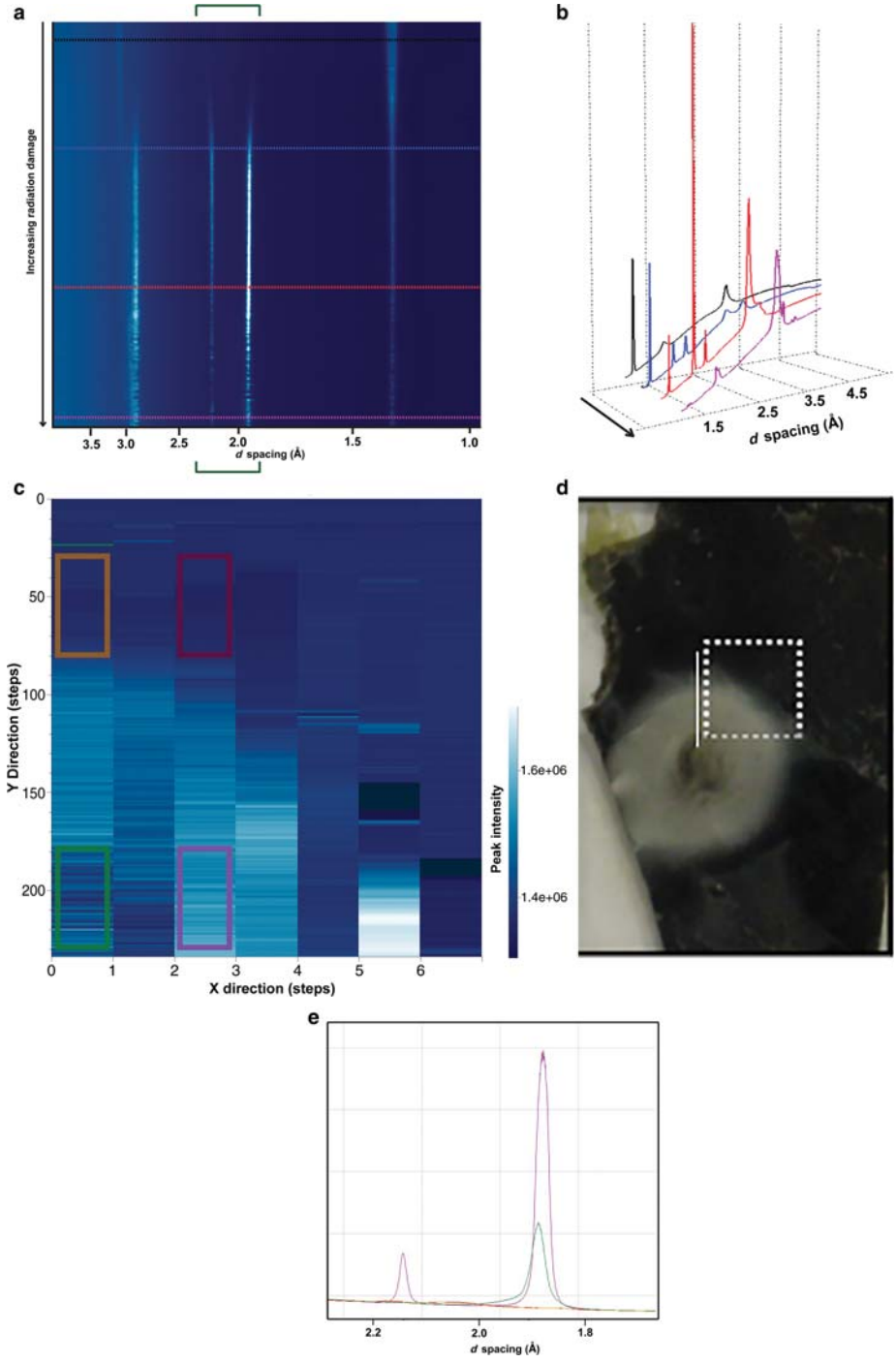
a
Increasing radiation damage
3.5
3.0
2.5
2.0
1.5
1.0
d spacing (Å)
b
1.5
2.5
3.5
4.5
d spacing (Å)
c
Y Direction (steps)
0
50
100
150
200
0
1
2
3
4
5
6
X direction (steps)
Peak intensity
1.6e+06
1.4e+06
d
e
2.2
2.0
1.8
d spacing (Å)

cases. One or two small catalyst particles were placed in a 300 μm glass capillary supported on glass wool. The capillary was mounted vertically on two mini translation stages on top of a rotation axis enabling placement of the sample in the center of rotation. The XRF tomography of the Pt catalyst particle was performed using a 2 μm × 2 μm beam by XRF mapping of the particle at 20.3 keV every 5° of rotation to produce 37 maps. Data analysis was performed using python scripts and then the TomoJ plug-in (Messaoudil *et al.,* 2007) in *ImageJ* (Schneider *et al.*, 2012). The XANES tomography of a single slice of the particle was performed by collecting XRF line scans across the particle at 37 different rotations at 80 separate incident energies about the Pt L_3 edge. This gave 80 sinograms which were centered before filter back-projection using an inverse RADON transformation to give real-space Pt fluorescence images. These images were stacked and then examined using the program *MANTIS* (Lerotic *et al.*, 2004). The μ-XRD-CT (μ-X-ray diffraction computed tomography) was performed on a Co/SiO_2 catalyst particle by collection of diffraction images at 13 keV at every point in a map of the particle (0.5 s per image). The XRD patterns were calibrated and integrated azimuthally using the program *DAWN* (Basham *et al.*, 2015). Each 2θ step in the reduced dataset was then filter-back projected to create the final 3D datastack having two spatial axes (*x, y*) with the 3rd axis (*z*) being the reconstructed pattern (2θ).

3. Results and discussion

3.1. Biotite

A one-dimensional (1D) plot showing the changes in XRD peak intensity *vs. d* spacing in a traverse into the center of the 6.5 mm silver circle of α particle damage in a crystal of biotite is shown in Figure 1a (see Figure 1d); three 1D plots were extracted from Figure 1a to show the XRD pattern at specific radiation doses (colored lines) in Figure 1b. The *d* spacings show that the lattice planes expand, contract, and split with increasing dose as the crystal accommodates increased defect densities; new peaks representing different lattice planes (and *d* spacings) emerge as the biotite breaks down into 'damage-induced' crystallites, revealing previously forbidden reflections. Ultimately, as the radiation damage increases and defects predominate, the peaks fade and become much more sporadic across the region analyzed.

Similar to the clay phase (detailed below), the interlayer reflection (~7.5 Å) shows a small shift to smaller *d* spacing (0.111 Å) in the irradiated zone (as shown by lab-based p-XRD). This interlayer contraction may have consequences for radionuclide ion

Figure 1. (a) XRD track into alpha-particle damaged biotite, showing change in peak position as radiation damage increases. (b) Individual 1D XRD patterns at the positions of the horizontal lines are shown. (c) Map of the intensity in the diffraction pattern in the *d* spacing range 1.7–2.3 Å heading into the center of the damage area. The step size was 30 μm in the Y direction and 1 mm in the X direction. (d) Photograph showing the sample, the approximate position of the line scan (a) and the area of the map (c). (e) Integrated 1D diffraction patterns from the colored boxes in part c.

uptake. A method using a map to show three-dimensional (3D) representations of structural changes is shown in Figure 1c; the map displays the integrated peak intensity in the *d* spacing range 11.4–15 Å for seven XRD traverses (patterns were collected at 30 μm intervals into the damage zone and at 1 mm intervals across the sample).

The sample and the map area are shown in Figure 1d. The paler blue area represents the in-growing peaks that emerge into the radiation-damaged zone. While there is a clear trend progressing into the damaged zone, the consistency of the intensities perpendicular to this is more sporadic; areas of greatest peak intensity are not necessarily next to each other, revealing the heterogeneity of radiation damage at this scale. The integrated 1D diffraction patterns from the colored regions in the map are also shown in Figure 1e to illustrate the peaks that are present only in the more damaged phase.

The average Fe K-edge XANES for three spectra collected adjacent to the XRD traverse in areas outside and inside the damage zone are shown in Figure 2. Trioctahedral micas contain mainly Fe(II); inconsistent octahedral layer occupancy in biotite (Vedder, 1969) results in dioctahedral domains across these layers, however, which will preferentially retain a small proportion of Fe(III). A small shift of the absorption edge to lower energy demonstrates some reduction of the iron with high ion doses. An Fe(III) to Fe(II) reduction mechanism as a result of α-particle irradiation of biotite was proposed by Pattrick *et al.* (2013), postulating that radiolysis of structural OH groups within the biotite structure liberates reducing electrons under ion bombardment.

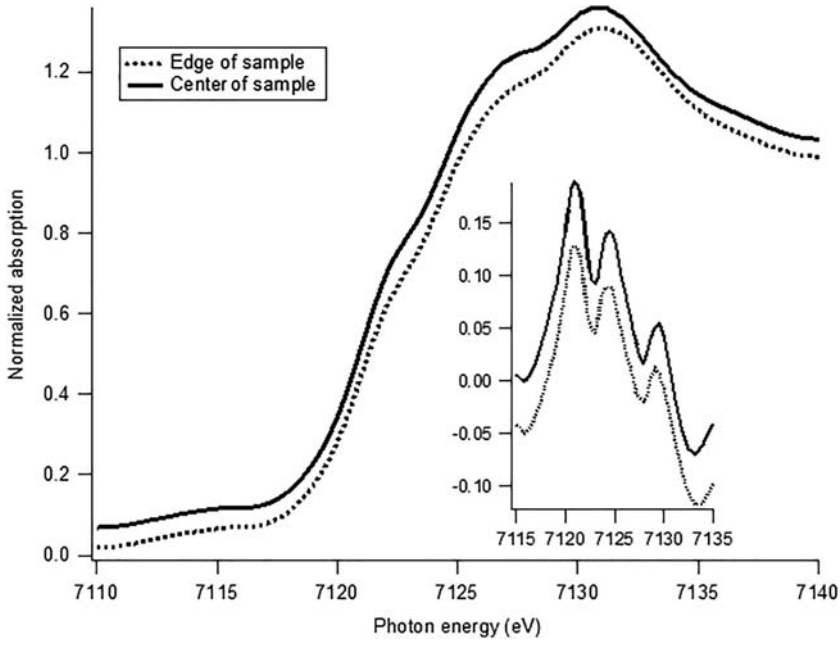

Figure 2. Normalized XANES spectra (each spectrum is the average of three individual traces) from the center and edge of the α particle-damaged biotite. Inset is the 1st derivative of the spectra.

3.2. Montmorillonite

The 1D plot in Figure 3 shows the effect of α-particle damage on the interlayer spacing in the montmorillonite SCa-3. The structure of montmorillonite (monoclinic) consists of two tetrahedral Si sheets surrounding one Al-containing octahedral sheet, plus the cation-filled interlayer. The basal spacing is defined as the d_{001} distance and this increases with hydration. The d_{001} distance measured from the diffuse rings in the XRD images collected in the un-irradiated zone is 14.1 Å, which agrees well with powder XRD data for an oriented SCa-3 aggregate. The effect of dose on the penetration depth of the $^4He^{2+}$ ions can be seen by the stark change in color on the back of the irradiated sample; in the center, where the dose is greatest, the $^4He^{2+}$ ions penetrate all the way through the sample resulting in the discoloration. Toward the edge of the beam profile, where the dose is lower, the $^4He^{2+}$ ions do not penetrate all the way through the sample and the discoloration can only be seen on the front of the irradiated sample. Where the $^4He^{2+}$ ions penetrate all the way through the sample, the change in the d_{001} distance to 9.5 Å is dramatic, indicating collapse of the interlayer as a result of $^4He^{2+}$ ion bombardment. This interlayer collapse will have a significant effect on the sorption capacity of the montmorillonite.

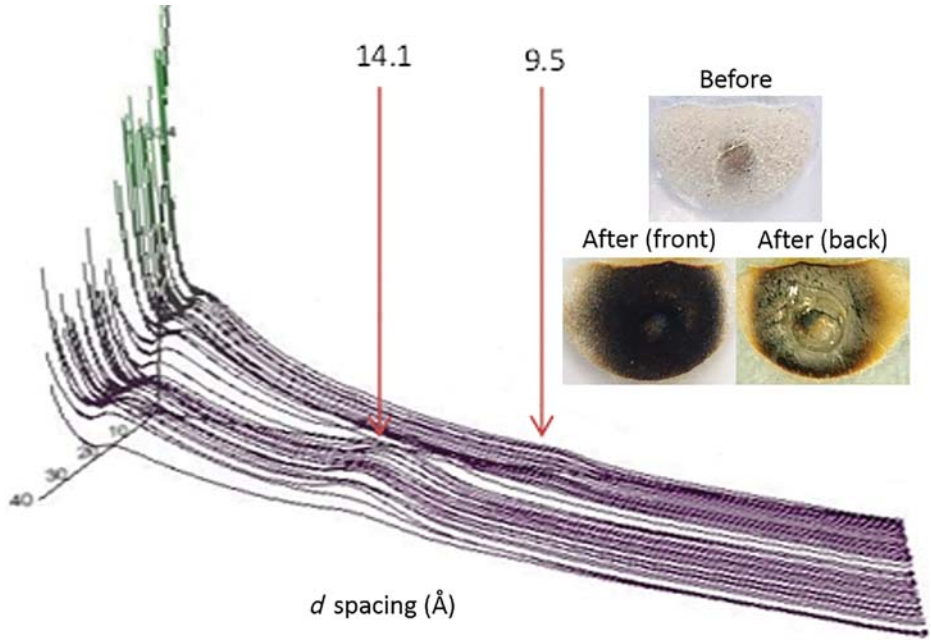

Figure 3. 1D XRD patterns collected at 75 μm intervals along a path in the α particle-damaged montmorillonite (SCa-3), showing a change in the interlayer spacing. The pattern at 0 is from the center of the damaged zone. Above are photographs of SCa-3 before and after α particle damage showing the difference in damage on the front and back of the clay.

3.3. Pt catalyst particle

The carbon framework supporting the Pt catalysts is from an activated carbon slurry which has a pore size of ~2 nm. Colloidal Pt is added from a solution of H_2PtCl_6 and hexadecyl(2-hydroxyethyl)dimethyl ammonium di-hydrogen-phosphate (HHDMA) (the latter controls the Pt cluster size). These colloidal clusters (~6 nm) are believed to be too big to penetrate the carbon and, thus, Pt is presumed to form a shell around the outside of the carbon particles. The Mo is added from an $(NH_4)_6Mo_7O_{24}.(H_2O)_4$ solution and is expected to permeate throughout the structure. Horizontal and vertical cross-sections of the particle are shown in Figure 4, a reconstruction from XRF tomography. The Mo distribution (green) is relatively even throughout the particle but the Pt (red) is concentrated around the edge; despite the colloidal control, however, a significant amount of Pt remains within the particle (Price *et al.*, 2015b). This Pt will be less active catalytically than the external Pt because the transport of the reactant through the carbon support will be very slow. Hence, the study has shown that not all the Pt in the catalyst is in an optimal location.

The XANES tomography was used to probe the chemistry of the carbon phase inside and on the surface of the particle. The images in Figure 5 show the results of cluster analysis on the non-normalized XANES cross-section. Bulk XANES and EXAFS studies suggested the Pt state was a mixture of 50% Pt(0) and 50% chlorinated Pt(II) species (Price *et al.,* 2015b). The edge positions in the cluster analysis are all identical and the difference is largely due to the amount of Pt (size of absorption edge). The high Pt loading shows more noise than the other three spectra extracted from the cluster (possibly due to problems in the reconstruction) but all four spectra have similar white lines and edge positions, suggesting that the chemical speciation of the Pt is similar throughout the particle, *i.e.* a mixed chloro metallic state. μXANES imaging is one of the few techniques able to probe such information from inside a particle.

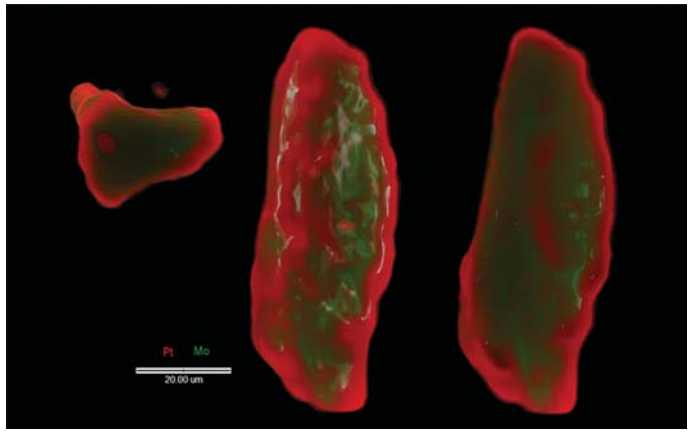

Figure 4. Surface (center image) and cross-sections (from the center) from XRF tomography showing Pt (red) and Mo (green) (left and right images, respectively) distributions on the carbon support.

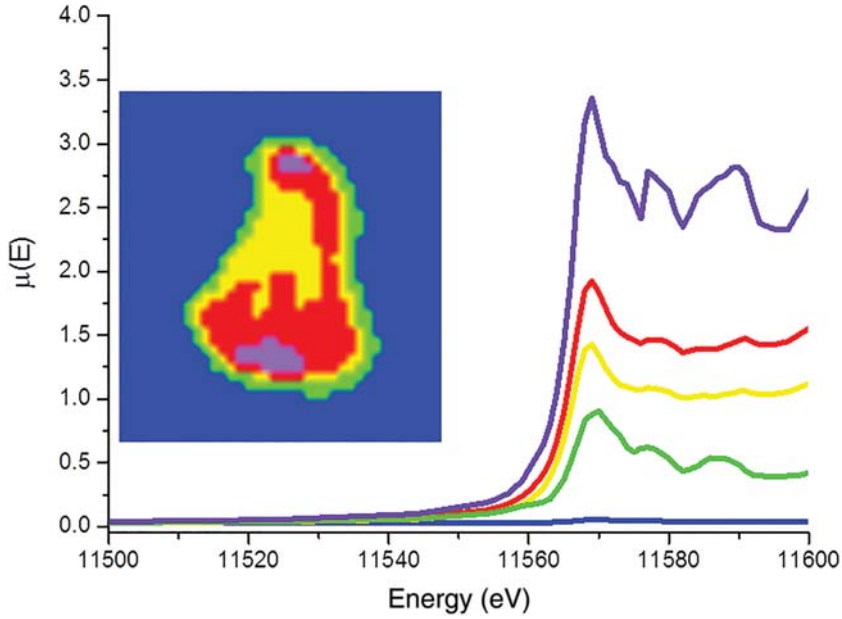

Figure 5. Cluster map of reconstructed Pt XANES tomography datastack (inset) and associated XANES spectra. The color of each spectrum corresponds to the color of the cluster in the cluster map. The blue spectrum is from outside the particle where no Pt is present (figure adapted from Price *et al.* (2015b) with the permission of the PCCP Owner Societies).

3.4. Co catalyst particle

Results from the μXRD-CT analysis of the Co catalyst particle are shown in Figure 6. The 1D diffraction patterns (Figure 6a) show that there are two separate cobalt oxide phases – CoO and Co_3O_4 and one TiO_2 (anatase) phase. A slice from the tomographic reconstruction (Figure 6b) shows that CoO is seen on the outside of the particle while Co_3O_4 is seen on the inside of the particle. Evidence of anatase in most of the particle is noted. The XRD of the as-prepared catalyst thus indicates that cobalt and titanium exist in separate phases, which is expected as they are deposited onto the silica sequentially (in this case, Ti followed by Co/Re). This example highlights spatial phase differences in the Co distribution that could not be determined easily by two-dimensional (2D) imaging.

4. Summary

The examples given here illustrate how synchrotron radiation imaging techniques can provide information not readily obtainable by other means. A particular strength of these studies is that one can 'resolve spatially' impurities/additional components

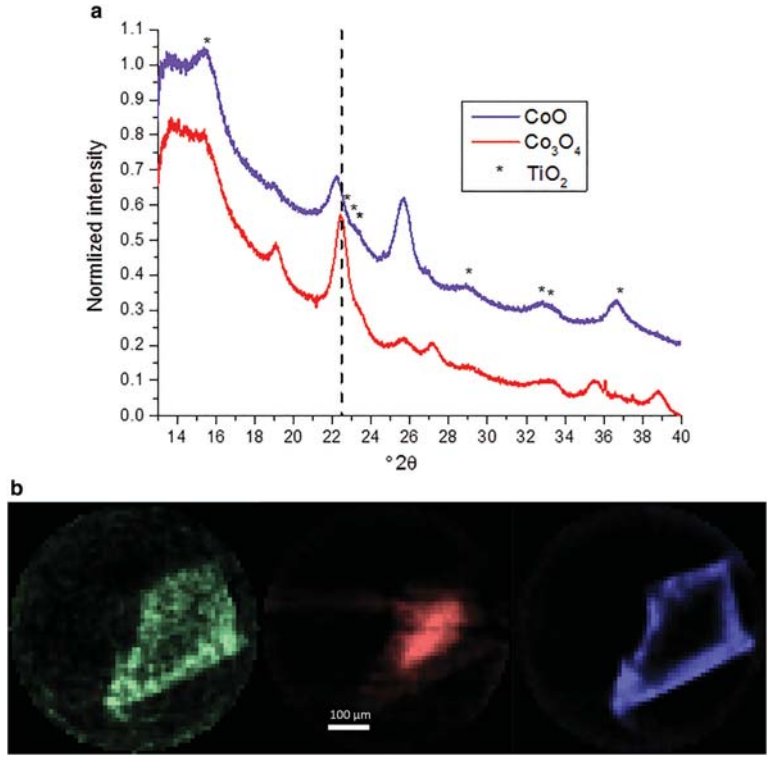

Figure 6. (a) 1D XRD traces from different voxels in 10 wt.% Co, 1 wt.% Re, 5 wt.% Ti/SiO_2. (b) Slices from the µXRD-CT reconstruction show the location of anatase (green), cobalt (II,III) oxide (red), and cobalt (II) oxide (blue) within the particle.

which are normally below the bulk-sampling detection limit. The mineralogical studies show how the structure of clay minerals and in particular their capacity to trap ions from solution is likely to alter after radiation damage (Bower *et al*., 2016). Thus these types of analyses can complement results from transmission electron microscopy where a much smaller sample may be imaged in atomic detail; the synchrotron techniques here provide information on how the short- and long-range order change at the micrometer scale. These changes may affect bulk properties such as adsorption. The catalyst examples demonstrate that similar information is available in 3D with suitable samples. Recent experiments on beamline I18 have extended these studies to catalysts under operating conditions, thus following structural and chemical changes while heating or adsorbing liquids is feasible (Price *et al.,* 2015a). Bulk techniques (*e.g.* XRD) measure an average of all the components within a sample; components with small contributions to the overall signal can be lost. The corresponding spatially resolved technique (*e.g.* XRD-CT) reveals these minor components and also their location with respect to the major components in the sample. Many catalysts are metal particles on a support; the location of the particles on the support can vary widely (*e.g.* homogenous, core-shell,

random) and this can affect the catalyst's performance. Using spatially resolved techniques in combination with, for example, mass spectrometry, identification of the location of the active material can be correlated to performance, enabling rational design of future catalysts.

A further advantage of 3D imaging over 2D imaging when combining μXANES or μXRF and μXRD techniques is that the potential difference in sampling volumes is eliminated; in order to achieve that, however, 3D studies require rather small samples. For XRD measurements, the energy may be chosen to suit the experiment; for the techniques using X-ray fluorescence, however, the energy of the fluorescence line is dependent on the element(s) being studied. Hence, the attenuation length of the material at the relevant energy must be considered when designing an experiment. For instance, the attenuation length of a standard biotite at the Fe Kα fluorescence line is ~40 μm, while just above the Fe K-edge (7112 eV) it is nearer to 30 μm (Hencke *et al.*, 1993). To study these materials in 3D by XAS methods requires particles which are no larger than ~80 μm, and even with that size self-absorption corrections must be made.

The recent advent of nano X-ray beamlines such as 26-ID-C at the Advanced Photon Source at Argonne National Laboratory (Chicago, Illinois, USA), ID16 at the E.S.R.F. (Grenoble, France), and P06 at Petra3 (Hamburg, Germany) makes the XRD and XRF techniques applicable on a smaller length scale than that demonstrated here. The number of points required in 3D XANES imaging and the variation in energy makes that a considerable challenge at the nanoscale.

Acknowledgments

The authors thank Peter Witte (BASF SE) for providing the Pt-Mo/C particle, Andy Smith and Simon Pimblott (DCF) for assistance with the pelletron experiments, Steve Stockley for preparation of the clay samples, David Martin (UCL) for assistance with Co particle measurement, and Mark Basham, Jake Filik, Tina Geraki, and Konstantin Ignatyev (Diamond Light Source) for help with various aspects of the data analysis. The Diamond Light Source is also acknowledged for providing the beamtime. AMB thanks EPSRC for funding (EP/K007467/1). William Bower is supported by NERC DTA at the University of Manchester.

Guest editor: H.C. Greenwell

The authors and editors are grateful to anonymous reviewers who offered very helpful input and suggestions. A list of all reviewers is given at the end of the Preface for this volume.

References

Allard, T. and Calas, G. (2009) Radiation effects on clay mineral properties. *Applied Clay Science*, **43**, 143–149.

Basham, M., Filik, J., Wharmby, M.T., Chang, P.C.Y., El Kassaby, B., Gerring, M., Aishima, J., Levik, K., Pulford, W.A.C., Sikharulidze, I., Sneddon, D., Webber, M. Dhesi, S.S., Maccherozzi, F., Svensson,

O., Brockhauser, S., Náray, G., and Ashton, A.W. (2015) Data Analysis WorkbeNch (DAWN). *Journal of Synchrotron Radiation* **22**, DOI: 10.1107/S1600577515002283.

Basile, F., Benito, P., Bugani, S., De Nolf, W., Fornasari, G., Janssens, K., Morselli, L., Scavetta, E., Tonelli, D., and Vaccari, A. (2010) Combined use of synchrotron-radiation-based imaging techniques for the characterization of structured catalysts. *Advanced Functional Materials*, **20**, 4117–4126.

Beale, A.M., Jacques, S.D.M., Gibson, E.K., and Di Michel, M. (2014) Progress towards five dimensional diffraction imaging of functional materials under process conditions. *Coordination Chemistry Reviews*, **277–278**, 208–223.

Bleuet, P., Welcomme, E., Dooryhee, E., Susini, J., Hodeau, J.-L., and Walter, P. (2008) Probing the structure of heterogeneous diluted materials by diffraction tomography. *Nature Materials*, **7**, 468–472.

Bower, W.R., Pearce, C.I., Smith, A.D., Pimblott, S.M., Mosselmans, J.F.W., Haigh, S.J., and Pattrick, R.A.D. (2015) Radiation damage in biotite mica by accelerated α-particles: a synchrotron microfocus X-ray diffraction and X-ray absorption spectroscopy study. *American Mineralogist*, **101**, 928–942.

Brinza, L., Schofield, P.F., Hodson, M.E., Weller, S., Ignatyev, K., Geraki, K., Quinn, P.D., and Mosselmans, J.F.W. (2014) Combining μXANES and μXRD mapping to analyse the heterogeneity in calcium carbonate granules excreted by the earthworm Lumbricus terrestris. *Journal of Synchrotron Radiation*, **21**, 235–241.

Fittschen, U.E.A. and Falkenberg, G. (2011) Trends in environmental science using microscopic X-ray fluorescence. *Spectrochimica Acta B: Atomic Spectroscopy*, **66**, 567–658.

Henke, B.L., Gullikson, E.M., and Davis, J.C. (1993) X-ray interactions: photoabsorption, scattering, transmission, and reflection at E = 50-30000 eV, Z = 1-92. *Atomic Data and Nuclear Data Tables*, **54**, 181–342.

Jacques, S.D.M., Di Michiel, M., Beale, A.M., Sochi, T., O'Brien, M.G., Espinosa-Alonso, L., Weckhuysen, B.M., and Barnes, P. (2011) Dynamic X-ray diffraction computed tomography reveals real-time insight into catalyst active phase evolution. *Angewandte Chemie-International Edition*, **50**, 10148–10152.

Leay, L., Bower, W.R., Horne, G., Wady, P., Baidak, A., Pottinger, M., Nancekievill, M., Smith, A.D., Watson, S., Green , P.R., Lennox, B., Laverne, J.A., and Pimblott, S.A. (2015) Development of irradiation capabilities to address the challenges of the nuclear industry. *Nuclear Instruments and Methods in Physics Research Section B: Beam Interactions with Materials and Atoms*, **343**, 62–69.

Lee, S.Y. and Tank, R.W. (1985) Role of clays in the disposal of nuclear waste: A review. *Applied Clay Science*, **1**, 145–162.

Lerotic, M., Jacobsen, C., Schäfer, T., and Vogt, S. (2004) Cluster analysis of soft X-ray spectromicroscopy data. *Ultramicroscopy*, **100**, 35–57.

Lombi, E. and Susini, J. (2009) Synchrotron-based techniques for plant and soil science: opportunities, challenges and future perspectives. *Plant Soil*, **320**, 1–35.

Marcus, M.A. (2010) X-ray photon-in/photon-out methods for chemical imaging. TrAC. *Trends in Analytical Chemistry*, 29, 508–517.

Materlik, G., Rayment, T., and Stuart, D.I. (2015) Diamond Light Source: status and perspectives. *Philosophical Transactions of the Royal Society of London A: Mathematical, Physical and Engineering Sciences*, **373**, 20130161.

Messaoudil, C., Boudier, T., Oscar Sanchez Sorzano, C., and Marco, S. (2007) TomoJ: tomography software for three-dimensional reconstruction in transmission electron microscopy. *BMC Bioinformatics*, **8**, 288.

Mosselmans, J.F., Quinn, P.D., Dent, A.J., Cavill, S.A., Moreno, S.D., Peach, A., Leicester, P.J., Keylock, S.J., Gregory, S.R., Atkinson, K.D., and Rosell, J.R. (2009) I18 - the microfocus spectroscopy beamline at the Diamond Light Source. *Journal of Synchrotron Radiation*, **16**, 818–824.

Pattrick, R.A.D., Charnock, J.M., Geraki, T., Mosselmans, J.F.W., Pearce, C.I., Pimblott, S.M., and Droop, G.T.R. (2013) Alpha particle damage in biotite characterised by microfocus X-ray diffraction and Fe K-edge X-ray absorption spectroscopy. *Mineralogical Magazine*, **77**, 2867–2882.

Peacock, C.L. and Moon, E.M. (2012) Oxidative scavenging of thallium by birnessite: explanation for thallium enrichment and stable isotope fractionation in marine ferromanganese precipitates. *Geochimica et Cosmochimica Acta*, **84**, 297–313.

Price, S.W.T., Geraki, K., Ignatyev, K., Witte, P.T., Beale, A.M., and Mosselmans, J.F.W. (2015a) In situ microfocus chemical computed tomography of the composition of a single catalyst particle during hydrogenation of nitrobenzene in the liquid phase. *Angewandte Chemie International Edition*, **54**, 9886–9889.

Price, S.W.T., Ignatyev, K., Geraki, K., Basham, M., Filik, J., Vo, N.T., Witte, P., Beale, A.M., and Mosselmans J.F.W. (2015b) Chemical imaging of single catalyst particles with scanning μ-XANES-CT and μ-XRF-CT. *Physical Chemistry Chemical Physics*, **17**, 521–529.

Ravel, B. and Newville, M. (2005) ATHENA, ARTEMIS, HEPHAESTUS: data analysis for X-ray absorption spectroscopy using IFEFFIT. *Journal of Synchrotron Radiation*, **12**, 537–541.

Rickwood, P.C. (1981) The largest crystals. *American Mineralogist*, **66**, 885–907.

Roqué-Rosell, J., Mosselmans, J.F.W., Proenza, J.A., Labrador, M., Galí, S., Atkinson, K.D., and Quinn, P.D. (2010) Sorption of Ni by "lithiophorite–asbolane" intermediates in Moa Bay lateritic deposits, eastern Cuba. *Chemical Geology*, **275**, 9–18.

Ruiz-Martinez, J., Beale, A.M., Deka, U., O'Brien, M.G., Quinn, P.D., Mosselmans, J.F.W., and Weckhuysen, B.M. (2013) Correlating metal poisoning with zeolite deactivation in an individual catalyst particle by chemical and phase-sensitive X-ray microscopy. *Angewandte Chemie-International Edition*, **52**, 5983–5987.

Savage, D. and Arthur, R. (2012) Exchangeability of bentonite buffer and backfill materials. STUK Radiation and Nuclear Safety Authority, Helsinki, p. 57.

Schneider, C.A., Rasband, W.S., and Eliceiri, K.W. (2012) NIH Image to ImageJ: 25 years of image analysis. *Nature Methods*, **9**, 671–675.

Vedder, W. (1969) Dehydroxylation and rehydroxylation, oxidation and reduction of mica. *American Mineralogist*, **54**, 482–509.